Impurity (Fe, Cl, and P)-Induced Grain Boundary and Secondary Phases in Commercially Pure Titanium (CP-Ti)

M. YAN, S.D. LUO, G.B. SCHAFFER, and M. QIAN

A detailed transmission electron microscopy (TEM) study has been made of the microstructures of two as-sintered CP-Ti materials. We show that iron content at the impurity level of 1280 ppm, less than the limit (2000 ppm) for CP-Ti ASTM Grade 1, is sufficient to lead to the formation of a grain boundary (GB) β-Ti phase in the as-sintered microstructure due to segregation. The Fe-stabilized GB β-Ti phase contains ~7 at. pct Fe and ~1.5 at. pct Cl. In addition, nano-precipitates of ω-Ti exist in the Fe-stabilized GB β-Ti phase. A phosphorus (P)-enriched Ti-P-based phase was also identified, which has a tetragonal crystal structure with lattice parameters of ($a = b = 8.0 \pm 0.2$ Å and $c = 2.7 \pm 0.2$ Å) and is new to the existing database for Ti-P-enriched phases. As-sintered CP-Ti materials are thus not necessarily a single α-Ti phase material. These impurity-induced phases may exert potential impacts on the properties of sintered CP-Ti.

DOI: 10.1007/s11661-013-1720-0

I. INTRODUCTION

DEPENDING on temperature and pressure, titanium can be stable as α-Ti (closed-packed hexagonal, cph), β-Ti (body-centred-cubic, bcc), or ω-Ti (simple hexagonal, h)[1–5]; their crystal structures are shown in Figure 1. The α–β transformation occurs at ~1155 K (882 °C) under atmospheric pressure, while the ω-Ti phase is usually regarded as a high-pressure (>2 GPa) and/or low-temperature [<−475 K (202 °C)] phase in pure Ti.[1–5]

The four grades of commercially pure titanium (CP-Ti) are classified according to their oxygen (O) and iron (Fe) contents with specified carbon (C) and nitrogen (N) contents. These impurities affect the mechanical and corrosion behaviors of CP-Ti materials, which, including their modified forms, account for ~25 pct of the current titanium market.

Powder-based approaches have received increasing attention in recent years as a cost-effective alternative to the fabrication of Ti products.[6–14] In particular, the cold-compaction-and-sinter powder metallurgy (PM) approach is technically the simplest and economically the most attractive near-net shape PM fabrication method, compatible with nonfatigue critical applications.[9] This is in addition to the constitutional (greater chemical homogeneity) and microstructural (finer grain size) attributes offered by this approach.[9] CP-Ti materials, irrespective of the fabrication route, are generally assumed to be as single-phase α-Ti materials.

M. YAN, Queensland Smart Future Fellow (Early Career), S.D. LUO, Postdoctoral Research Fellow, G.B. SCHAFFER, Professor, and M. QIAN, Reader in Materials, are with The University of Queensland, School of Mechanical and Mining Engineering, ARC Centre of Excellence for Design in Light Metals, Brisbane, QLD 4072, Australia. Contact e-mail: m.yan2@uq.edu.au
Manuscript submitted April 19, 2012.
Article published online April 10, 2013

This study presents a detailed TEM analysis of the microstructures of two as-sintered CP-Ti materials containing 40 ppm and 1280 ppm of Fe. We show that the microstructure of a CP-Ti material can be a complex mixture of phases. The implications of the findings are discussed.

II. EXPERIMENTAL

AEE-Ti powder (prepared by plasma spray and supplied by Atlantic Equipment Engineers; to be denoted as high-Fe CP-Ti powder) and WUYI-Ti powder (hydride–dehydride powder, supplied by Kemit Special Metal Powder; to be denoted as low-Fe CP-Ti powder) were used. Impurities of these two powders were analyzed by various means (Model Leco TC-436 for O, SPECTRO ICP-OES.09 for Fe and METROHM 751 TITRINO for Cl and P). The results are summarized in Table I. The Fe content is lower than the limit (2000 ppm) for CP-Ti ASTM Grade 1.

Titanium powder was uniaxially pressed into cylinders of 10 mm in both diameter and height at 800 MPa. The sample preparation details can be found elsewhere.[15] Sintering was conducted at 1623 K (1350 °C) for 60 minutes in an alumina-tube vacuum furnace. The vacuum pressure was in the order of 10^{-2} Pa during isothermal sintering at 1623 K (1350 °C). Heating and cooling were both carried out at 4 °C/min. All the sintered samples achieved >95 pct of theoretical density, when measured by the Archimedes method.

TEM was used to analyze the microstructure including phase identification, assisted by XRD. Samples for TEM (Tecnai F20, operated at 200 kV) analysis were thinned by a twin-jet polishing apparatus at 243 K (−30 °C), using a mixed solution of 60 pct methanol + 35 pct 2-butoxyethanol + 5 pct $HClO_4$ (all in vol. pct) as the electrolyte. Selected-area-electron

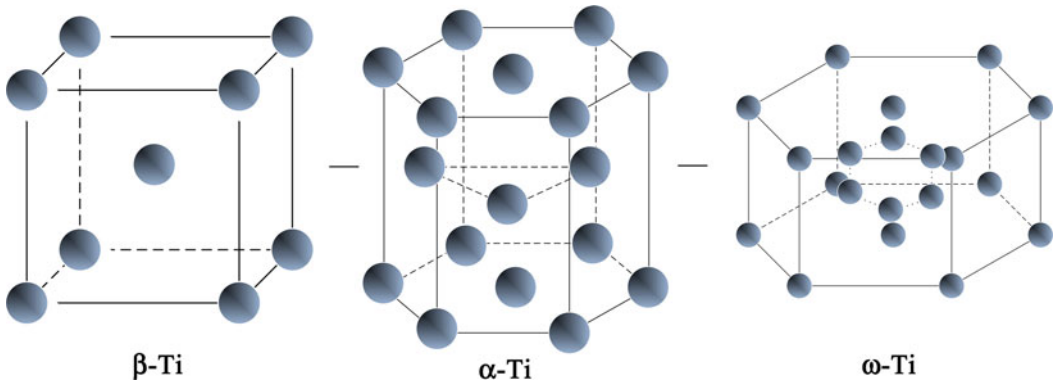

Fig. 1—Illustration of the crystal structures of α-Ti, β-Ti, and ω-Ti.

Table I. Impurity Contents of the Low-Fe and High-Fe CP-Ti Powders (in Wt Pct)

Supplier	Production Method	O	Fe	Cl	P
WUYI-Ti	hydride–dehydride	0.360	0.004	0.025	<0.005
AEE-Ti	plasma spray	0.690	0.128	0.008	<0.005

diffraction (SAED) and convergent-beam-electron diffraction (CBED) were used to determine the crystal structure. TEM electron-dispersive-spectrometer (TEM-EDX) was used to analyze the phase constitution, and the energy resolution of the TEM-EDX used is in the order of 1 eV. XRD was conducted on a Bruker D8 Advance diffractometer with a Cu K*a* target operating at 40 kV and 60 mA. Thermo-Calc Software and Ti-alloy database V3 (TTTI3) were used to acquire the phase and solubility information in Ti-Fe and Ti-O systems.

III. RESULTS

A. *Preliminary Characterization of As-Sintered CP-Ti Materials*

Figure 2 shows the XRD spectra for the as-sintered high-Fe and low-Fe CP-Ti samples. Only the α-Ti phase (see Figure 1) was detected. The TEM bright-field (BF) image (Figure 3(a)) displays a few typical Ti grain boundaries (GBs) in the as-sintered low-Fe Ti powder. The CBED results (Figures 3(b) and (d)) confirmed that these are the GBs between α-Ti grains, and the GBs show the same crystal structure as the neighboring α-Ti grains (see Figure 3(c)). These are the expected GBs in a typical CP-Ti material (*i.e.*, low-Fe). For this type of GB, the misorentation between the neighboring Ti grains is normally smaller than 11 deg (*e.g.*, ~2.0 deg between the Grain 1 and Grain 2 as indicated in the figure), suggesting that they are small-angle grain boundaries (SAGBs). A majority of the GBs observed in the as-sintered high-Fe CP-Ti sample are similar to those shown in Figure 3.

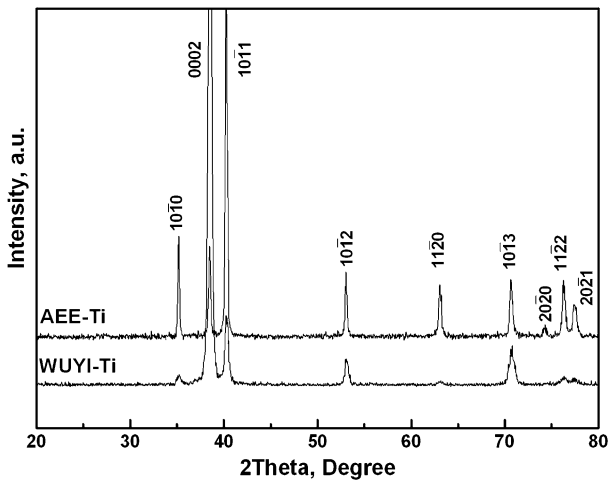

Fig. 2—XRD results for the as-sintered high-Fe CP-Ti and low-Fe CP-Ti samples. Only the α-Ti phase was detected in both materials.

B. *Fe-Induced GB Phases in the As-Sintered High-Fe CP-Ti*

A closer TEM observation of the GBs in the as-sintered high-Fe Ti sample revealed the presence of a GB phase. Figures 4(a) and (b) show two of such observations. The corresponding SAED patterns in the inset show overlap of diffraction patterns arising from both the α-Ti matrix and the GB phase. Figures 4(c) and (d) further indicate that the misorientation angle between the two neighboring α-Ti grains is significant (~67 deg in this case), suggesting that it is a large-angle grain boundary (LAGB). Normally, LAGB corresponds to high interface energy which may induce the precipitation of a GB phase. The thickness of the GB phase is in the range of 80 to 200 nm. About 10 pct of those the GBs show such a GB phase. A noticeable presence of Fe, O, and Cl was detected in the GB phase by TEM-EDX (see Figure 5(a)). Figure 5(b) shows the TEM-EDX results obtained from five different GB phases in one TEM sample. The Fe content (~7 at. pct) and Cl content (~1.5 at. pct) are generally consistent while the oxygen content shows large variations. Some of these

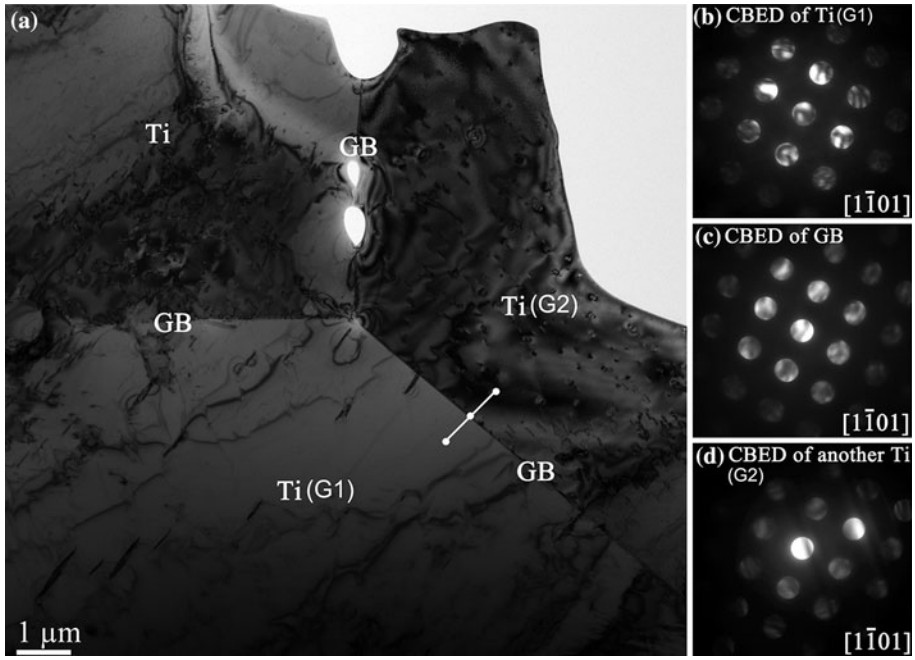

Fig. 3—(*a*) TEM-BF image and (*b*) to (*d*) CBED patterns for the α-Ti matrix and normal grain boundaries observed in an as-sintered low-Fe Ti sample. G1 and G2 stand for Grain 1 and Grain 2, respectively.

phases are essentially oxygen free (~0.5 at. pct) whereas others are oxygen enriched (~25 at. pct). It should be noted that the thickness of these GB phases (80 to 200 nm) are much greater than that of the oxide film (<8 to 10 nm[12]) detected on bulk Ti or Ti powder surfaces. The oxide film will dissolve into the underneath Ti matrix at greater than ~700 °C because of the significant solubility of oxygen in Ti.[9]

Figure 6 shows the TEM-SAED patterns of a GB phase. The crystal structure is body-centred-cubic (bcc) with a lattice parameter, $a = 3.3 \pm 0.1$ Å, consistent with the bcc β-Ti phase ($a = 3.3$ Å). Fe is a β-Ti stabilizer.[1,2] The Fe-containing GB phase was observed only in the as-sintered high-Fe CP-Ti which contains 1280 ppm Fe. The as-sintered low-Fe Ti samples contain 40 ppm Fe and are free of GB phases. Thermo-Calc calculations predict that the solubility limit of Fe in α-Ti at room temperature is ~200 ppm, higher than the Fe content in the low-Fe Ti powder, but much lower than the Fe content (1280 ppm) in the high-Fe Ti powder. This indicates that the formation of the GB phase in the as-sintered high-Fe Ti sample is induced by the segregation of Fe to the GB area. The GB phase is thus identified to be an Fe-stabilized β-Ti phase (see Figure 1). High-resolution TEM (HRTEM) revealed the interfacial bonding condition between the GB β-Ti phase and the α-Ti matrix (Figures 7(a) and (b)), suggesting good GB β-Ti/α-Ti matrix bonding with an orientation relationship of $(10\bar{1}0)_{\alpha\text{-Ti}}//(12\bar{1})_{GB}$; $[0\bar{1}10]_{\alpha\text{-Ti}}//[012]_{GB}$.

The SAED patterns of the Fe-stabilized GB β phase show additional features in certain zone axes besides the regular diffraction spots, such as those shown in Figures 6(c) and (e) at the zone axes of [112] and [110]. These additional features are ring-shaped diffuse scattering, shown approximately in the positions of (111), (201), (001), and (111) in the corresponding SAED patterns (Figures 6(d) and (f)). They are one of the so-called Relrod shapes in reciprocal space, corresponding to spherical particles in real space.[16] This is illustrated in Figures 8(a) through (d). Figure 8(d), a TEM dark-field (TEM-DF) image, shows the presence of superfine nanoparticles or clusters (~1 to 3 nm) in the GB β-Ti phase, responsible for the diffuse scattering recorded by the SAED patterns. The corresponding TEM-BF image is shown in Figure 8(c). These superfine nanoparticles in the β-Ti phase may be ω-Ti nanoprecipitates.[3,17,18] It is known that the ω-Ti phase is less stable in oxygen-enriched beta phases.[3,17,18] In this study, the ω-Ti precipitates were observed in various β-Ti phases containing oxygen from <2 at. pct to about 20 at. pct (Figure 5b), while the α-Ti matrix close to the grain boundary (GB) β-Ti phases typically contains 3 to 4 at. pct by the TEM EDX analyses. The high oxygen content in some of the GB β-Ti phases is likely due to surface contamination.

C. *A phosphorous (P)-Enriched Phase in the As-Sintered High-Fe CP-Ti*

The detailed TEM study has also found another phase in the as-sintered high-Fe CP-Ti, shown in Figures 9(a) and (b). The phase is ~50 to 200 nm in size and contains a significant amount of phosphorous (P) and a certain amount of O as shown by TEM-EDX (see Figure 9(b)).

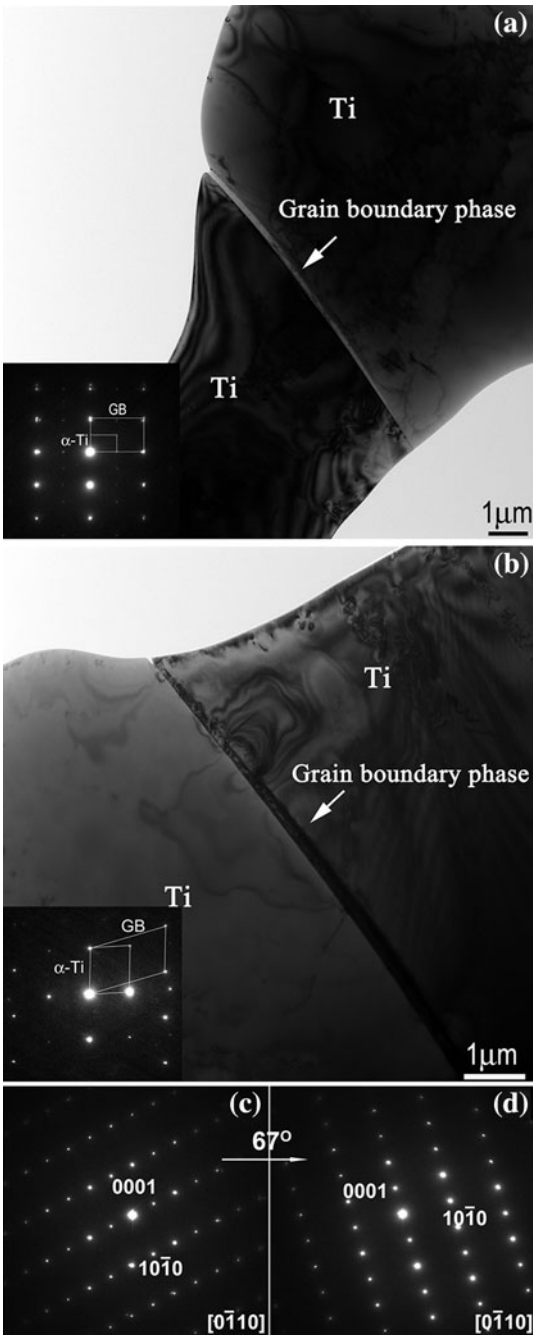

Fig. 4—(*a*) and (*b*) TEM-BF images for the grain boundary phases observed in the as-sintered high-Fe Ti sample. Insets show SAED patterns from both the α-Ti matrix and the GB phase. (*c*) and (*d*) are [0$\bar{1}$10] patterns of the two grains which were obtained by tilting ~67 deg angle within TEM.

Its composition is close to $Ti_{79.7}P_{14.0}O_{6.3}$ (in at. pct; accuracy ± 10 pct), which differs from the α-Ti matrix. A comparative spectrum from the α-Ti matrix is also provided in Figure 9(b).

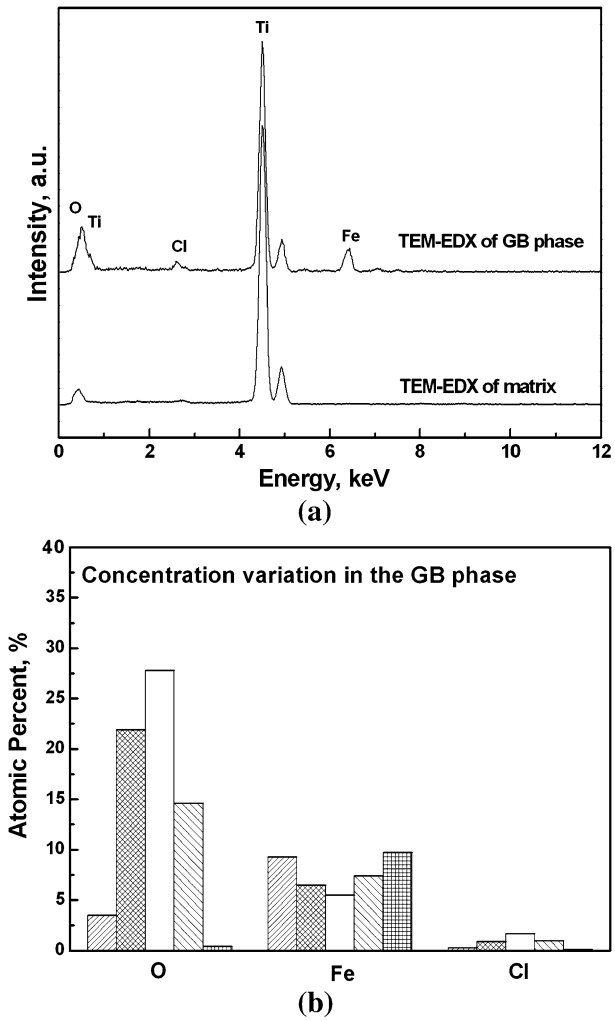

Fig. 5—(*a*) TEM-EDX results for grain boundary phase analyzed in the as-sintered high-Fe Ti showing the presence of O, Fe, and Cl; the EDX spectrum of the Ti matrix is also shown for comparison, and (*b*) impurity contents obtained from analyzing five grain boundary phases.

The SAED patterns in Figure 10 reveal that the phase shows a 4-fold symmetry but it is not a cubic phase judging from the tilting angles between the SAED patterns obtained (*i.e.*, the angles between these zone axes). The extra diffraction spots in the figure are from neighboring grains but they have no effect on the analysis of the phase. It is a tetragonal-structured phase with lattice parameters of $a = b = 8.0 \pm 0.2$ Å, and $c = 2.7 \pm 0.2$ Å. The HRTEM image of this phase, obtained at the zone axis of [00$\bar{4}$] and shown in Figure 11, displays its atomic image as well as its bonding with the neighboring α-Ti grain, where the SAED patterns of the α-Ti grain are indexed into its [44$\bar{0}$0] zone axis, and there is an orientation relationship between the two phases: $(000\bar{4})_{\alpha\text{-Ti}}//(220)_{\text{P-rich}}$ and

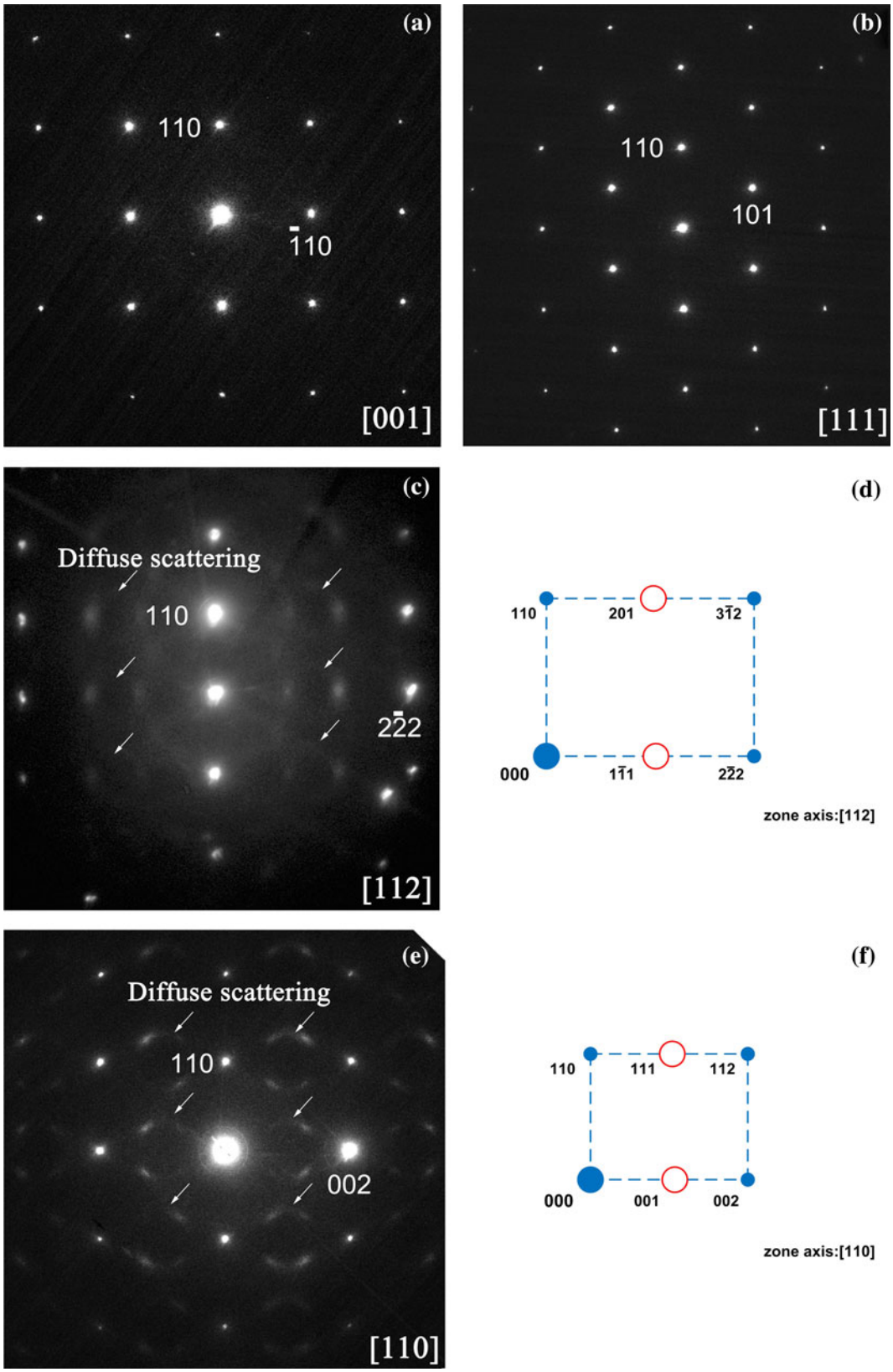

Fig. 6—(*a*), (*b*), (*c*) and (*e*) are TEM analyses of the GB phase (*i.e.*, Fe-stabilized β-Ti). The GB phase shows normal electron diffraction at certain zone axes like the [001] and [111]. Extra electron diffraction features are observed at, *e.g.*, [112] and [110] zone axes. These extra features are analyzed in detail in (*d*) and (*f*).

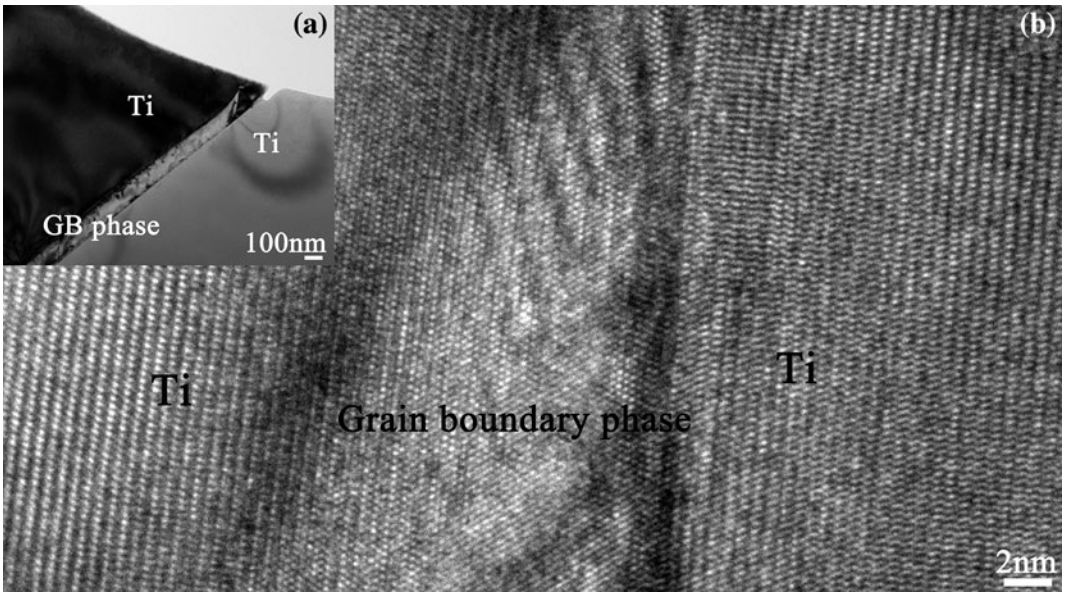

Fig. 7—(*a*) TEM-BF image and (*b*) the corresponding HRTEM image to reveal the bonding between the GB phase and the α-Ti matrix.

$[4\bar{4}00]_{\alpha\text{-Ti}}//[00\bar{4}]_{\text{P-rich}}$. A survey of the phases in the binary (Ti-P) and ternary (Ti-P-O) systems suggests that the phase has not previously been reported. There are 67 space groups under the category of tetragonal crystal system. Based on the reflections shown by the P-rich phase (see Figure 10), those body-centred space groups, such as I4 and I4/mmm, are excluded, for they only allow reflections from the spots of $h + k + l = 2n$ (n is integral and hkl are plane indexes).[19] The overall concentration of P in the high-Fe and low-Fe Ti is <50 ppm (Table I).

IV. IMPLICATIONS OF THE FINDINGS

The TEM analysis detailed above has shown that impurities, especially those of Fe, O and P, have changed the microstructure of CP-Ti from a single α phase to a complex mixture of

- α-Ti (as majority);
- grain boundary β-Ti phase (observed at ~10 pct of the grain boundaries);
- ω phase inside the β-Ti; and
- a P-enriched secondary phase (of limited number).

It is noted that the Fe content (1280 ppm) examined in the high-Fe powder is clearly less than the limit (2000 ppm) set for CP-Ti ASTM Grade 1, while the phosphorus content is at a trace level (<50 ppm). They are typical of many CP-Ti materials. The prime applications of CP-Ti materials, including the modified Ti-(0.15 to 0.20)Pd (Grades 7 and 11) alloys, are largely based on their excellent corrosion resistance. Beta-Ti (β-Ti) normally shows less corrosion resistance than α-Ti.[1,2] In addition, the presence of the GB β-Ti phase creates new interfaces in the as-sintered microstructure. Hence the formation of the GB β-Ti phase plus the P-enriched Ti-P-O phase may be detrimental to the corrosion resistance. It has been suggested that low iron and interstitial contents of ASTM CP-Ti Grade 1 might enhance corrosion resistance.[20] The TEM findings of this study suggest that the Fe content in CP-Ti materials may need to be stringently controlled for demanding corrosion-resistant applications.

On the other hand, Fe is an inexpensive β-Ti stabilizer. For this reason, there has been an increasing interest in the development of low-cost and high-performance Ti-Fe-based PM Ti alloys.[21–23] This study shows that Fe is very effective in promoting the formation of β phase in PM Ti materials; the presence of 1280 ppm Fe can lead to the formation of β-Ti. This can be used as a starting point for the estimate of the Fe content needed in PM Ti-Fe-based alloy design.

Contrary to Fe and Cl, phosphorus (P) is an uncommon impurity in CP-Ti and Ti alloys. It is not specified in the chemistry for CP-Ti materials. The origin of the P in the high-Fe samples is unclear; it might originate from the steel vessels in the Kroll process or during powder preparation by the plasma-spray approach.[24] The solubility of P in solid-sate titanium is very low,[25,26] ~70 ppm (0.007 wt pct) at 1063 K (790 °C),[26] and is lower at room temperature. It is thus reasonable that P is present in the form of Ti-P compounds. As a result, a trace amount of P may be used as a grain growth inhibitor in Ti where Ti-P precipitates may curb the growth of the β-Ti grains during sintering or heat treatment.[26] This study confirms that a trace amount of P (<50 ppm) is sufficient to induce the formation of a Ti-P-based

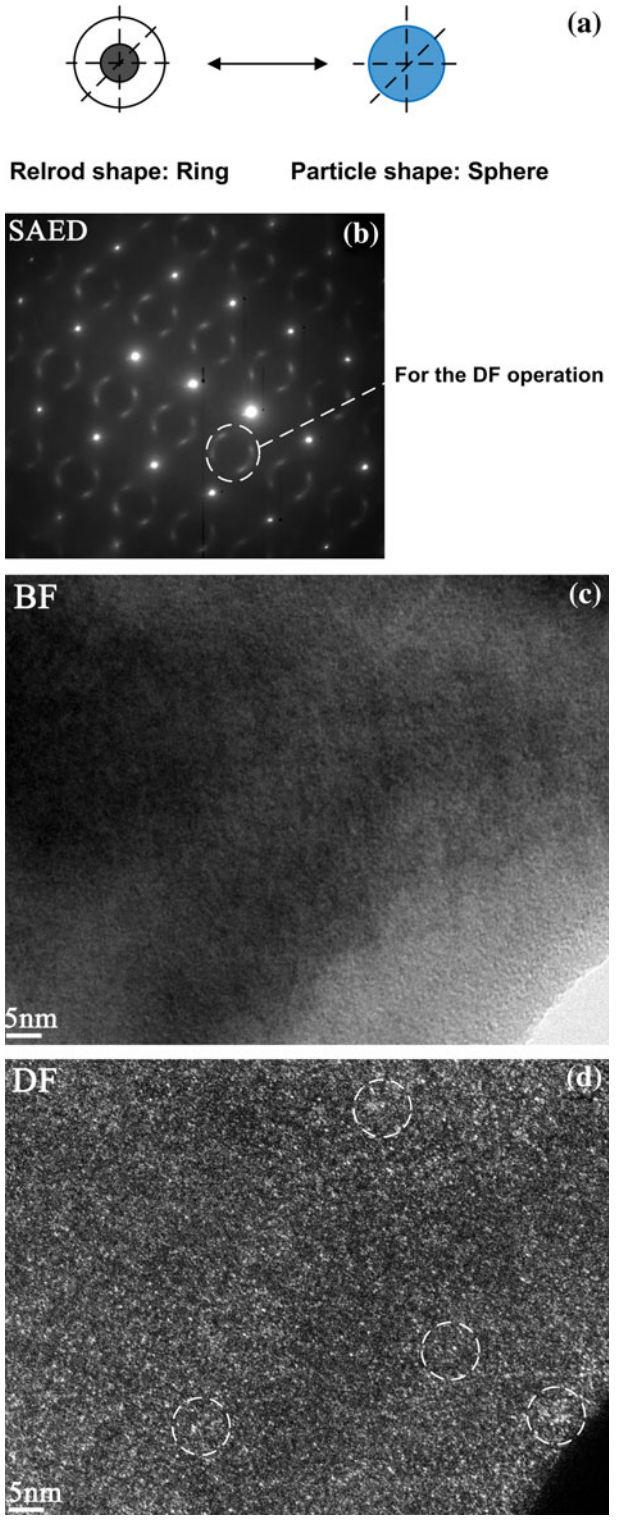

Fig. 8—TEM analyse of the nanoprecipitates in the grain boundary phase: (*a*) correlation between the relrod shape (in the reciprocal space) and the particle shape (in the real space), (*b*) the corresponding SAED pattern for the BF (*c*) and DF (*d*) images, and (*d*) nanoparticles revealed by the DF image.

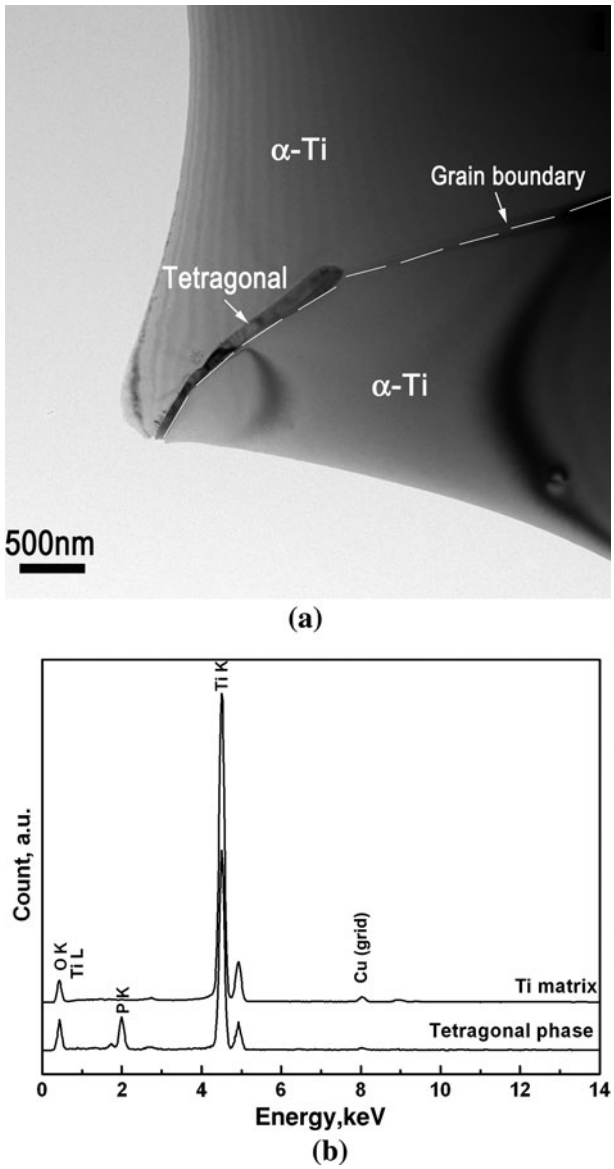

Fig. 9—(*a*) TEM-BF image of the P-enriched tetragonal phase, and (*b*) the TEM-EDX analyses of the α-Ti matrix and the P-enriched phase.

secondary phase in the as-sintered CP Ti. In addition, the Ti-P phase observed is located at the grain boundary area (Figure 9), suggesting that P may be used as a potential grain growth inhibitor as proposed previously.[26]

V. SUMMARY

Owing to impurities, as-sintered CP-Ti materials can have complex phase constituents rather than a single α phase as typically assumed. The presence of Fe at the level of 1280 ppm is sufficient to induce a grain boundary (GB) β-Ti phase in the as-sintered microstructure. The GB β phase further contains superfine (1 to 3 nm) ω-Ti nano-precipitates. A trace amount of phosphorus (<50 ppm) in the Ti powder is capable of inducing the formation of a tetragonal-structured $Ti_{79.7}P_{14.0}O_{6.3}$ phase with lattice parameters of $a = b = 8.0 \pm 0.2$ Å, and $c = 2.7 \pm 0.2$ Å. These

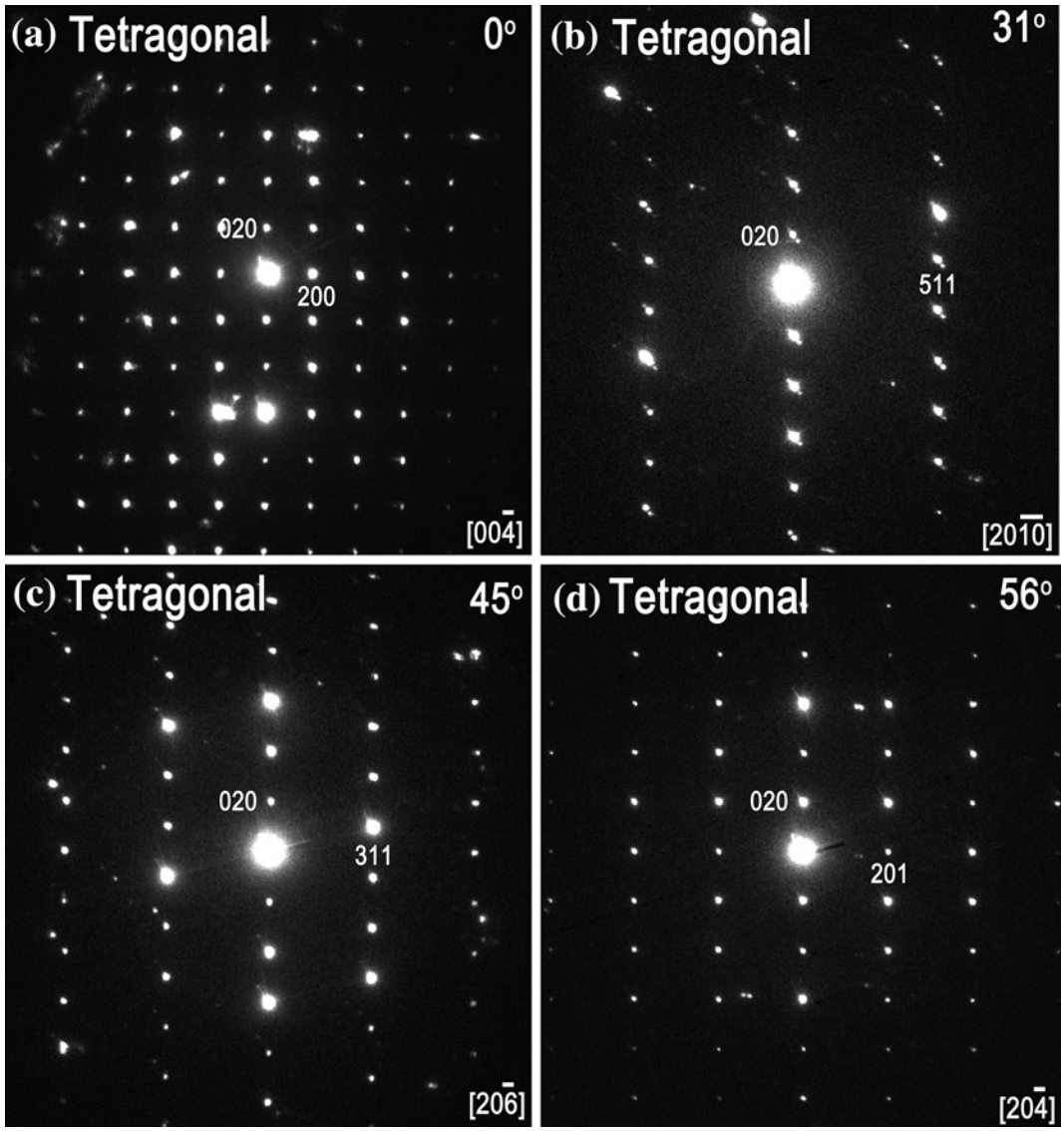

Fig. 10—(*a*) to (*d*) TEM-SAED analyses of the P-enriched tetragonal phase: the tilting angles recorded between these SAED patterns.

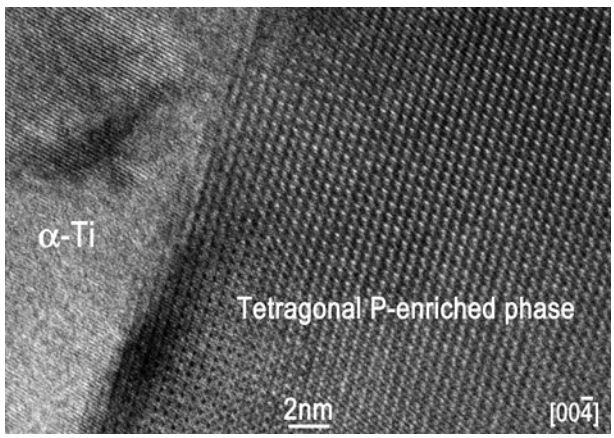

Fig. 11—HRTEM image of the P-enriched tetragonal phase obtained at the [00$\bar{4}$] zone axis.

microstructural changes may lead to the reduced corrosion resistance of the CP-Ti materials. The identification of the $Ti_{79.7}P_{14.0}O_{6.3}$ phase supports a previous hypothesis that phosphorus has the potential to be a grain growth inhibitor in Ti.

ACKNOWLEDGMENTS

This work was funded by the Australian Research Council (ARC) through the Centre of Excellence for Design in Light Metals. Dr. M. Yan acknowledges the support of the Queensland Smart Futures Fellowship (Early Career). Discussion with Prof. Jim Williams of The Ohio State University about the nature of the grain boundary phase and its formation is acknowledged. The constructive and in-depth suggestions received from the reviewer are acknowledged.

REFERENCES

1. G. Lutjering and J.C. Williams: *Titanium*, 2nd edn., Springer, 2007.
2. C. Leyens and M. Peters eds.: *Titanium and Titanium Alloys: Fundamentals and Applications,* Wiley, Weinheim, 2003.
3. S. Banerjee and P. Mukhopadhyay: *Phase Transformations, Volume 12: Examples from Titanium and Zirconium Alloys (Pergamon Materials Series)*, 1st edn., Elsevier, 2005.
4. R.G. Hennig, D.R. Trinkle, J. Bouchet, S.G. Srinivasan, R.C. Albers, and J.W. Wilkins: *Nat. Mater.*, 2005, vol. 4, pp. 129–33.
5. H. Conrad: *Prog. Mater. Sci.*, 1981, vol. 26, pp. 123–404.
6. J.C. Williams and E.A. Starke: *Acta Mater.*, 2003, vol. 51, pp. 5775–99.
7. T. Saito: *JOM*, 2004, vol. 56, pp. 33–36.
8. Y. Liu, L.F. Chen, H.P. Tang, C.T. Liu, B. Liu, and B.Y. Huang: *Mater. Sci. Eng., A*, 2006, vol. 418, pp. 25–35.
9. M. Qian: *Inter. J. Powder Metall.*, 2010, vol. 46, pp. 29–44.
10. M. Yan, Y. Liu, Y.B. Liu, C. Kong, G.B. Schaffer, and M. Qian: *Scripta Mater.*, 2012, vol. 67, pp. 491–94.
11. M. Yan, Y. Liu, G.B. Schaffer, and M. Qian: *Scripta Mater.*, 2013, vol. 68, pp. 63–66.
12. I.M. Robertson and G.B. Schaffer: *Powder Metall.*, 2010, vol. 53, pp. 146–62.
13. M. Ashraf Imam: *JOM*, 2011, vol. 63, pp. 16–23.
14. S.D. Luo, M. Yan, G.B. Schaffer, and M. Qian: *Metall. Mater. Trans. A*, 2011, vol. 42A, pp. 2466–74.
15. M. Yan, S.D. Luo, G.B. Schaffer, and M. Qian: *Mater. Lett.*, 2012, vol. 72, pp. 64–67.
16. D.B. Williams and C.B. Carter: *Transmission Electron Microscopy*, New York, Plenum Press, 1996.
17. A. Devaraj, R.E.A. Williams, S. Nag, R. Srinivasan, H.L. Fraser, and R. Banerjee: *Scripta Mater.*, 2009, vol. 61, pp. 701–704.
18. X.H. Wu, J. del Prado, Q. Li, A. Huang, D. Hu, and M.H. Loretto: *Acta Mater.*, 2006, vol. 54, pp. 5433–48.
19. Th. Hahn, ed.: *International Tables for Crystallography Volume A: Space-Group Symmetry*, First online edition, 2006, http://it.iucr.org/Ab/.
20. R. Boyer, G. Welsch, and E.W. Collings: *Materials Properties Handbook: Titanium Alloys,* ASM International, Materials Park, 1994, p. 165.
21. B.Y. Chen, K.S. Hwang, and K.L. Ng: *Mater. Sci. Eng. A*, 2011, vol. 528, pp. 4556–63.
22. P.G. Esteban, E.M. Ruiz-Navas, and E. Gordo: *Mater. Sci. Eng. A*, 2010, vol. 527, pp. 5664–69.
23. Y.F. Yang, S.D. Luo, G.B. Schaffer, and M. Qian: *Metall. Mater. Trans. A*, 2012, in press.
24. Suryanarayanan: *Plasma Spraying: Theory and Applications,* World Scientific, Singapore, 1993.
25. H. Okamoto: *Phase Diagrams for Binary Alloys,* Materials Park, OH, 2000.
26. M. Marty, H. Octor, A. Walder, and L. les Roses: United States Patent No. 4,601,874, 1986.